



Synthesis, structure, and nonlinear optical property of $\text{Bi}_{0.33}\text{Sb}_{0.67}\text{SI}$

HPSTAR
1283-2021



Baixin Peng^{a,b,1}, Xiangli Che^{a,f,1}, Mengjia Luo^{a,b}, Dong Wang^d, Yang Wang^{a,b}, Yuhao Gu^e, Fuqiang Huang^{a,c,f,*}

^a State Key Laboratory of High-Performance Ceramics and Superfine Microstructure, Shanghai Institute of Ceramics, Chinese Academy of Sciences, Shanghai, 200050, China

^b University of Chinese Academy of Sciences, Beijing, 100049, China

^c State Key Laboratory of Rare Earth Materials Chemistry and Applications, College of Chemistry and Molecular Engineering, Peking University, Beijing, 100871, China

^d Center for High Pressure Science and Technology Advanced Research, Beijing, 100094, China

^e The Institute of Physics, Chinese Academy of Sciences, Beijing, 100190, China

^f CAS Center for Excellence in Superconducting Electronic (CENSE), Shanghai, 200050, China

ARTICLE INFO

Keywords:

SbSI
Nonlinear optics
Bi doping
Chalcohalide

ABSTRACT

The phase transition of SbSI from non-centrosymmetry to centrosymmetry occurs at 292K, which is too low for its practical applications such as ferroelectricity and nonlinear optics. Here, the substitution of Sb by Bi atoms is proposed to improve its phase transition temperature. A new chalcohalide, $\text{Bi}_{0.33}\text{Sb}_{0.67}\text{SI}$, has been successfully synthesized by self-flux method. It crystallizes in the non-centrosymmetric space group $Pmc2_1$ (No. 26) with $a = 4.1190$ (9) Å, $b = 10.225$ (2) Å, $c = 8.5318$ (18) Å. Different from the crystal structure of SbSI, $\text{Bi}_{0.33}\text{Sb}_{0.67}\text{SI}$ is composed of two kinds of edge-sharing distorted square pyramid $[\text{MS}_3\text{I}_2]^{5-}$ ($M = \text{Bi}$ or Sb), which form $[\text{M}_2\text{S}_4\text{I}_2]^{4-}$ chains along a axis. The compound exhibits a moderate powder second harmonic generation signal at 2.09 μm, which was consistent with its non-centrosymmetric structure.

1. Introduction

Non-centrosymmetric (NCS) compounds with intrinsic dipole moment have a wide range of applications such as ferroelectric device [1–4], piezoelectric [5–7] and pyroelectric sensor [8–11], and infrared laser [12–15]. Introducing polar structural units is a common practice to achieve the NCS compounds [16,17], but it's difficult to control the spatial arrangement of polar structural units. In addition, solid solution is a useful method to get the NCS compounds through inducing phase transition from centrosymmetry to non-centrosymmetry [18]. For example, orthorhombic ($Pnma$) to tetragonal ($I4_1md$) phase transition can be induced in anti-perovskite phosphide $(\text{Ca}_{1-x}\text{Sr}_x)\text{Pd}_3\text{P}$ when $x \geq 0.6$ [20]. Furthermore, superconductivity is induced in the range of $0.17 \leq x \leq 0.55$ [20].

SbSI is a ferroelectric semiconductor with a Curie point at about 292 K [21,22]. The ferroelectric phase $Pna2_1$ and paraelectric phase $Pnam$ of SbSI are investigated by Atsushi Kikuchi et al., in 1967 [22]. The difference between the two phases is caused by shifting of Sb and S along

ferroelectric c axis [22]. Furthermore, due to its high values of electro-mechanical coefficient and piezoelectric coefficient, SbSI is very attractive for piezoelectric generators [23–25]. However, SbSI can only keep NCS structure below 292 K, which limits its practical application at higher temperature. Hence, there is a need to increase its Curie temperature.

In this paper, Bi-doping was proposed to increase the curie temperature of SbSI. A new compound $\text{Bi}_{0.33}\text{Sb}_{0.67}\text{SI}$ with NCS structure $Pmc2_1$ was successfully synthesized by introducing Bi into SbSI using self-flux method. The crystal structure is confirmed by single-crystal X-ray diffraction. The NCS compound $\text{Bi}_{0.33}\text{Sb}_{0.67}\text{SI}$ exhibits moderate powder SHG response under the laser radiation of 2.09 μm. The element ratio and phase purity of $\text{Bi}_{0.33}\text{Sb}_{0.67}\text{SI}$ were confirmed by energy dispersive X-ray spectroscopy (EDXS) and powder X-ray diffraction (PXRD), respectively. The band structure of $\text{Bi}_{0.33}\text{Sb}_{0.67}\text{SI}$ was analyzed by solid-state ultraviolet–visible (UV–vis) light diffuse-reflectance spectra and density functional theory (DFT) calculation. The infrared window of $\text{Bi}_{0.33}\text{Sb}_{0.67}\text{SI}$ was measured through infrared spectrophotometer.

* Corresponding author. State Key Laboratory of High-Performance Ceramics and Superfine Microstructure, Shanghai Institute of Ceramics, Chinese Academy of Sciences, Shanghai, 200050, China.

E-mail address: huangfq@mail.sic.ac.cn (F. Huang).

¹ Co-first author: Baixin Peng and Xiangli Che contribute equally to this work.

2. Methods

2.1. Synthesis

$\text{Bi}_{0.33}\text{Sb}_{0.67}\text{SI}$ was synthesized by self-flux reaction. Black single crystals scaling up to 60 μm were obtained (Figure S1b). The following reagents were used: Bi (99.999%, Alfa Aesar Puratronic), Sb (99.999%, Alfa Aesar Puratronic), S (99.999%, Alfa Aesar Puratronic) and I_2 (99.999%, Alfa Aesar Puratronic). Each reagent was weighed according to the molar ratio Bi: Sb: S: $\text{I}_2 = 0.33 : 0.67 : 1 : 0.5$, which is the best molar ratio to obtain pure phase. The total mass was controlled at 310 mg. They were mixed uniformly and encapsulated in a pre-evacuated quartz tube. The tubes are held at 973K for 48 h and reduced to 472 K with a cooling rate 42 K/h, and then cooled to room temperature with the furnace cooling to obtain single crystals sample. After the sample was taken out and mashed, it was added to a beaker containing 100 ml of aqueous solution of alcohol (volume ratio 1 : 1) and stirred with a magnetic stirrer for 0.5–1 h to remove by-products BiI_3 , SbI_3 , and I_2 remaining in the reaction. Finally, the product was separated by suction filtration and dried in an oven at 353 K to obtain the nonlinear optical crystal material. The attempt to synthesize $\text{Bi}_x\text{Sb}_{1-x}\text{SI}$ with other molar ratios of Bi: Sb was failed, since it's difficult to obtain pure phase.

2.2. Single-crystal X-ray diffraction

Well-grown single crystal was picked out for single-crystal X-ray diffraction. Crystallographic data was collected on a Bruker D8 QUEST diffractometer equipped with Mo $K\alpha$ radiation under room temperature. The crystal structures were solved and refined using APEX3 program [26]. Absorption corrections were performed using the multiscan method (ASDABS). The crystal structure and refinement details are summarized in Table 1.

2.3. Characterization

The obtained crystals were investigated with a JEOL (JSM6510) scanning electron microscope equipped with energy dispersive X-ray spectroscopy (EDXS, Oxford Instruments). X-ray diffraction data of the $\text{Bi}_{0.33}\text{Sb}_{0.67}\text{SI}$ samples were collected on a Bruker D8 Advance diffractometer equipped with mirror-monochromated Cu $K\alpha$ radiation ($\lambda = 0.15406 \text{ nm}$). The patterns were recorded in a slow-scanning mode with 2θ from 5° to 95° at a scan rate of $4^\circ/\text{min}$. Simulated patterns were obtained by using the mercury program and CIF file of the refined single-crystal structure. The solid-state ultraviolet–visible (UV–vis) light diffuse-reflectance spectra of the pure $\text{Bi}_{0.33}\text{Sb}_{0.67}\text{SI}$ powder was measured on a UV-4100 spectrophotometer operating from 1200 to 350 nm at room temperature. The IR optical measurements were carried

Table 1
Crystal data and structure refinement for $\text{Bi}_{0.33}\text{Sb}_{0.67}\text{SI}$.

chemical formula	$\text{Bi}_{0.33}\text{Sb}_{0.67}\text{SI}$
F_w (g/mol)	309.43
λ (Å)	0.71073
space group	$Pmc2_1$
a (Å)	4.1190 (9)
b (Å)	10.225 (2)
c (Å)	8.5318 (18)
V (Å ³)	359.32 (13)
Z	4
crystal color	black
μ (mm ⁻¹)	30.20
crystal size (mm ³)	0.104 × 0.087 × 0.042
no. of measured, independent, and observed $[I > 2\sigma(I)]$ reflections	1941, 689, 578
R_{int}	0.028
R [$F > 2\sigma(F)$], wR (F^2), GOF	0.022, 0.037, 1.11

$$^a R_1 = \frac{\sum ||F_o| - |F_c||}{\sum |F_o|}, ^b wR_2 = \frac{\{\sum [w(F_o^2 - F_c^2)]^2\}}{\sum [w(F_o^2)]^2}^{1/2}, w = 1/[\sigma^2(F_o) + (0.1000P)^2], \text{ where } P = (F_o + 2F_c)/3.$$

out at room temperature with an IR Prestige 21 Fourier transform infrared spectrophotometer in the range of 400–4000 cm^{-1} .

2.4. Second harmonic generation (SHG) measurement

The second harmonic generation response of $\text{Bi}_{0.33}\text{Sb}_{0.67}\text{SI}$ powder was measured by Kurtz Perry method [27] with a 2.09 μm Q-switch Ho/Tm/Cr/YAG laser in reflection mode. The sample and AgGaS_2 powder used for the measurement are full-size.

2.5. Density functional theory (DFT) calculation

We employed the Vienna ab initio simulation package (VASP) [28] code with the projector augmented wave (PAW) method [29] to perform our DFT calculation. The Perdew-Burke-Ernzerhof (PBE) [30] exchange-correlation functional was used in our calculations. The spin-orbital interactions were included in pseudopotentials. The kinetic energy cutoff is set to be 400 eV for the expanding the wave functions into a plane-wave basis. The internal atomic positions were relaxed until the force is less than 0.01 eV/Å. The energy convergence criterion was 10^{-6} eV and the Γ -centered k-mesh was set as $6 \times 8 \times 9$.

3. Results and discussion

3.1. Crystal structure of $\text{Bi}_{0.33}\text{Sb}_{0.67}\text{SI}$

$\text{Bi}_{0.33}\text{Sb}_{0.67}\text{SI}$ crystallizes in the polar orthorhombic space group $Pmc2_1$. The crystal structure is shown in Fig. 1. $\text{Bi}_{0.33}\text{Sb}_{0.67}\text{SI}$ contains two independent Bi/Sb site (2a, 2b), two independent I site (2a, 2b) and two independent S site (2a, 2b). The basic building units of this structure are two kinds of edge-sharing distorted square pyramid $[\text{MS}_3\text{I}_2]^{5-}$ ($M = \text{Bi}$ or Sb) (Fig. 1c), which are aligned nearly anti-parallel along the crystallographic a axis to construct $[\text{M}_2\text{S}_4\text{I}_2]^{4-}$ chains (Fig. 1d). These chains interact with each other through van der Waals force. The interaction of M and I between adjacent chains are indicated by dotted lines (Fig. 1c). The M atom forms a five-coordinate distorted pyramid structure with three S atoms and two I atoms. and the M site is randomly occupied by 1/3 Bi and 2/3 Sb respectively. The orderly arrangement of the basic building unit $[\text{MS}_3\text{I}_2]^{5-}$, acting as NLO active unit, is responsible for the observed SHG response.

The structure of $\text{Bi}_{0.33}\text{Sb}_{0.67}\text{SI}$ is similar to SbSI (Fig. 1a and b), which also presents a one-dimensional chain structure. But $\text{Bi}_{0.33}\text{Sb}_{0.67}\text{SI}$ crystallizes in $Pmc2_1$, while the latter crystallizes in $Pnam$. The $[\text{Sb}_2\text{S}_4\text{I}_2]^{4-}$ chains in SbSI are composed of two identical edge-sharing distorted square pyramid $[\text{SbS}_3\text{I}_2]^{5-}$, which align in an anti-parallel manner along a axis. The inversion center is located inside the $[\text{Sb}_2\text{S}_4\text{I}_2]^{4-}$ chains. The Sb1–S1, Sb2–S2 and Sb1–I1 distance are 2.70(43) Å, 2.46(02) Å, 3.12(32) Å, respectively [31]. Compared to Sb^{3+} , the introduction of Bi^{3+} with larger ionic radius and electron cloud density can generate stronger structure distortion. Thus, the bond lengths between M, S and I change accordingly. For M1 site, M1–S1, M1–S2 and M1–I2 distances are 2.50(75) Å, 2.17(87) Å, 3.14(62) Å, respectively. For M2 site, M2–S1, M2–S2 and M2–I1 distances are 2.73(35) Å, 2.54(01) Å, 3.15(25) Å, respectively. The coordination configuration of metal atoms is shown in Fig. 1c. The basic building units of $\text{Bi}_{0.33}\text{Sb}_{0.67}\text{SI}$ are two different distorted square pyramid $[\text{MS}_3\text{I}_2]^{5-}$, which causes the absence of inversion center in $\text{Bi}_{0.33}\text{Sb}_{0.67}\text{SI}$. The M–I and I–I distance between adjacent two chains in $\text{Bi}_{0.33}\text{Sb}_{0.67}\text{SI}$ are 3.76(57) Å and 4.06(08) Å, respectively, which is closer than Sb–I (3.83(34) Å) and I–I (4.06(57) Å) distance in SbSI, indicating that the structure of $\text{Bi}_{0.33}\text{Sb}_{0.67}\text{SI}$ is more densely packed than SbSI. Accordingly, the atom packing factors of $\text{Bi}_{0.33}\text{Sb}_{0.67}\text{SI}$ (0.170) are bigger than that of SbSI (0.168).

The powder X-ray diffraction pattern (Fig. 2) of the as-prepared $\text{Bi}_{0.33}\text{Sb}_{0.67}\text{SI}$ sample match well with the simulated PXRD pattern,

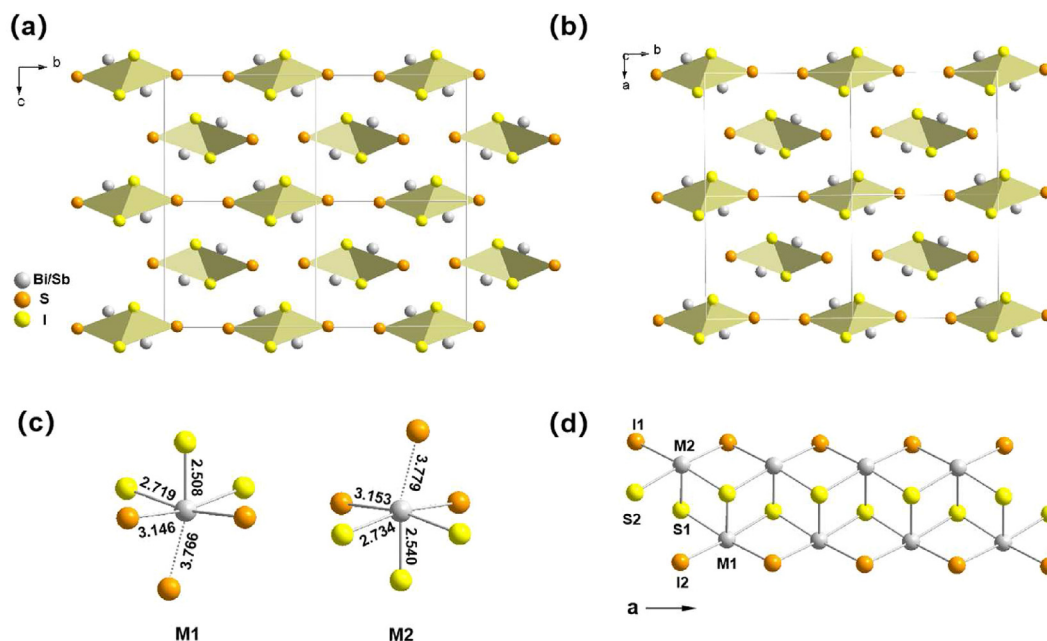


Fig. 1. (a) The crystal structure of $\text{Bi}_{0.33}\text{Sb}_{0.67}\text{SI}$ viewed down a axis, (b) The crystal structure of SbSI viewed down the c axis, (c) Coordination environment of metal atoms in $[\text{MS}_3\text{I}_2]^{5-}$ motifs of $\text{Bi}_{0.33}\text{Sb}_{0.67}\text{SI}$. (d) $[\text{M}_2\text{S}_4\text{I}_2]^{4-}$ chain of $\text{Bi}_{0.33}\text{Sb}_{0.67}\text{SI}$ along a axis.

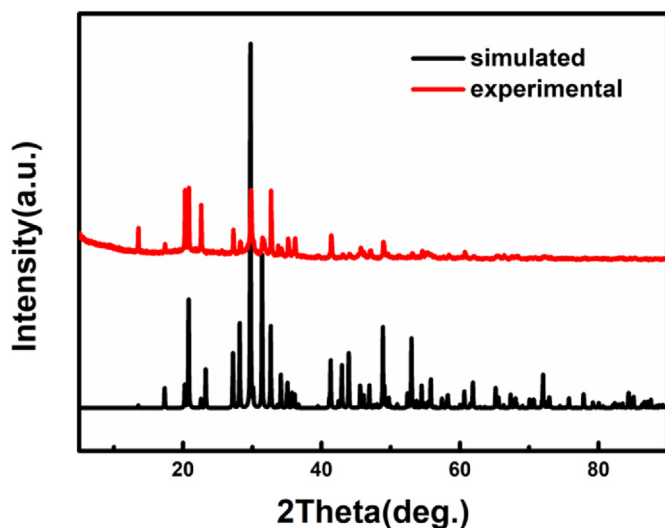


Fig. 2. Powder X-ray diffraction pattern of $\text{Bi}_{0.33}\text{Sb}_{0.67}\text{SI}$.

which indicates the sample is pure-phase. The SEM image shows the rod-like shape of the $\text{Bi}_{0.33}\text{Sb}_{0.67}\text{SI}$ crystal (Figure S1b), The element mapping shows that Bi, Sb, S and I elements are uniformly distributed in $\text{Bi}_{0.33}\text{Sb}_{0.67}\text{SI}$ (Figure S1a). The Bi/Sb/S/I ratio confirmed by semi-quantitative energy dispersive X-ray analysis (EDX) is 1/1.73/2.22/2.73, which is consistent with result of the Single-crystal X-ray Diffraction.

3.2. Optical properties

The UV–vis diffuse reflection spectrum of $\text{Bi}_{0.33}\text{Sb}_{0.67}\text{SI}$ is shown in Fig. 3a. Absorbance data were converted by the Kubelka-Munk function to evaluate their band gaps. The experimental band gap of $\text{Bi}_{0.33}\text{Sb}_{0.67}\text{SI}$ is estimated to be 1.7 eV, which is smaller than the parent compound SbSI (1.9 eV). The obvious difference between them can be explained by the smaller electronegativity of Bi element. The band structure of

$\text{Bi}_{0.33}\text{Sb}_{0.67}\text{SI}$ can be further elucidated by following electronic structure calculation. The IR spectrum indicate that there is no IR absorption result from the vibration of chemical bonds in a range of 5–25 μm (Fig. 3b).

DFT calculations was carried out to better understand the electronic band structure and the origin of SHG effect of $\text{Bi}_{0.33}\text{Sb}_{0.67}\text{SI}$. The band structure shows that $\text{Bi}_{0.33}\text{Sb}_{0.67}\text{SI}$ is an indirect-band-gap semiconductor with a bandgap of 1.22 eV (Fig. 3c). The semiconducting nature of $\text{Bi}_{0.33}\text{Sb}_{0.67}\text{SI}$ is simple: the valence of Bi/Sb/S/I are +3/+3/-2/-1, respectively. As a result, the p valence manifold of Bi/Sb is separated from the s valence manifold. The valence-band maximum (VBM) dominantly consists of S 3p and I 5p states, while the conduction-band minimum (CBM) is mainly composed of Bi 5p states as well Sb 4p states, as shown in Fig. 3d.

3.3. Second-harmonic generation measurement

The SHG signal of the polycrystalline powder of $\text{Bi}_{0.33}\text{Sb}_{0.67}\text{SI}$ was measured with the use of a laser at 2.09 μm as the fundamental wavelength. The SHG signal intensity is 0.12 times that of AgGaS_2 (AGS) with the same full particle size (Fig. 4).

The modest NLO response of $\text{Bi}_{0.33}\text{Sb}_{0.67}\text{SI}$ may be explained based on the macroscopic arrangement of the microscopic NLO-active building blocks. As shown in Fig. 1d, the one-dimensional chains along a axis are formed by two distorted square pyramid anion clusters $[\text{MS}_3\text{I}_2]^{5-}$, which are connected through edge-sharing in an anti-parallel way. The anti-parallel arrangement of $[\text{MS}_3\text{I}_2]^{5-}$ counteract the dipole moment, thus reducing the second-order susceptibility of $\text{Bi}_{0.33}\text{Sb}_{0.67}\text{SI}$ and leading to a relatively weak SHG response.

4. Conclusions

In summary, we have successfully designed and synthesized a new NCS metal chalcocyanide $\text{Bi}_{0.33}\text{Sb}_{0.67}\text{SI}$, which crystallized in the orthorhombic $Pmc2_1$ space group. The structure of $\text{Bi}_{0.33}\text{Sb}_{0.67}\text{SI}$ is composed of two kind of edge-sharing distorted square pyramid $[\text{MS}_3\text{I}_2]^{5-}$ ($M = \text{Bi}$ or Sb), which are arranged anti-parallel along the crystallographic a axis to form a 1D $[\text{M}_2\text{S}_4\text{I}_2]^{4-}$ chain. The macroscopic arrangement of the microscopic NLO-active building blocks $[\text{MS}_3\text{I}_2]^{5-}$ result in the modest NLO response of $\text{Bi}_{0.33}\text{Sb}_{0.67}\text{SI}$. According to UV–vis–NIR spectroscopy

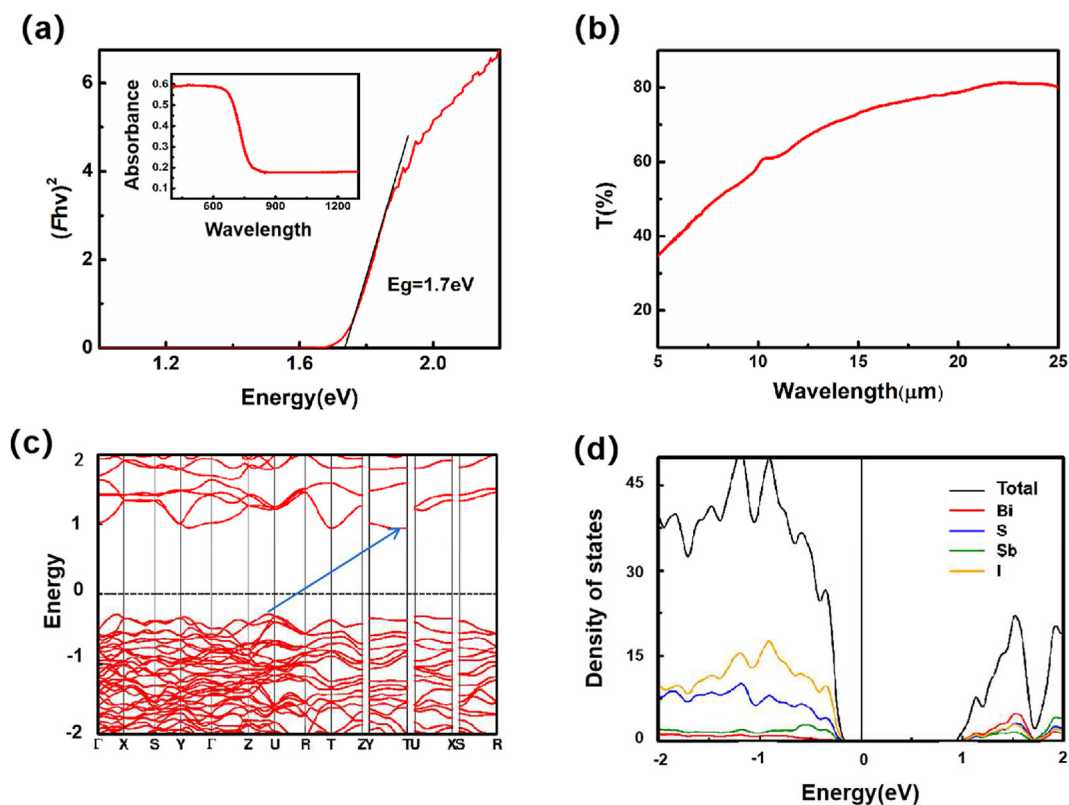


Fig. 3. (a) UV-vis Diffuse reflectance spectrum of $\text{Bi}_{0.33}\text{Sb}_{0.67}\text{SI}$. (b) Infrared spectrum of $\text{Bi}_{0.33}\text{Sb}_{0.67}\text{SI}$. (c) The band structure of $\text{Bi}_{0.33}\text{Sb}_{0.67}\text{SI}$. (d) DOS/PDOS of $\text{Bi}_{0.33}\text{Sb}_{0.67}\text{SI}$.

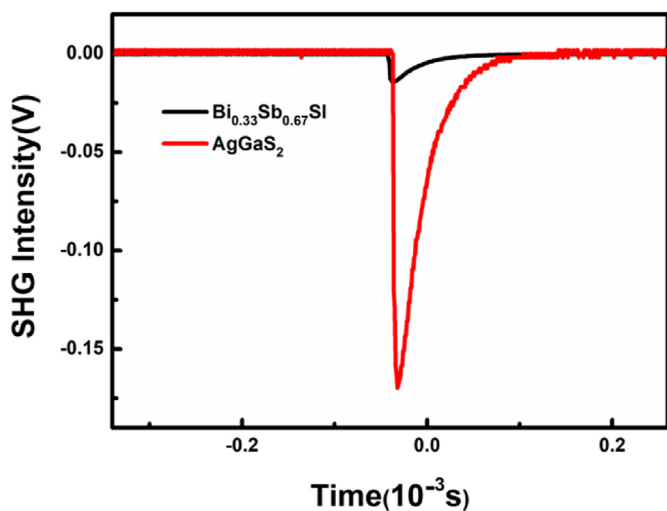


Fig. 4. SHG signals for $\text{Bi}_{0.33}\text{Sb}_{0.67}\text{SI}$ of full particle size with AgGaS_2 as a reference.

measurement, the band gap of $\text{Bi}_{0.33}\text{Sb}_{0.67}\text{SI}$ is about 1.7 eV, and the IR spectrum shows no IR absorption in a range of 5–25 μm .

CRediT authorship contribution statement

Baixin Peng: Investigation, Writing – original draft. **Xiangli Che:** Investigation, Validation. **Mengjia Luo:** Methodology. **Dong Wang:** Investigation. **Yang Wang:** Writing – original draft. **Yuhao Gu:** Formal analysis. **Fuqiang Huang:** Supervision.

Declaration of competing interest

The authors declare that they have no known competing financial interests or personal relationships that could have appeared to influence the work reported in this paper.

Acknowledgment

This work was financially supported by the Key Research Program of Chinese Academy of Sciences (Grants QYZDJ-SSW-JSC013 and KGZD-EW-T06), Innovation Project of Shanghai Institute of Ceramics (Grant No. Y93ZC2120G and No. E01ZC1110G) and sponsored by Shanghai Sailing Program (Grant 18YF1427200). The authors thank Min Luo from Fujian Institute of Research on the Structure of Matter for helpful nonlinear optical testing.

Appendix A. Supplementary data

Supplementary data to this article can be found online at <https://doi.org/10.1016/j.jssc.2021.122505>.

References

- [1] M. Li, H. Tan, W. Duan, Hexagonal rare-earth manganites and ferrites: a review of improper ferroelectricity, magnetoelectric coupling, and unusual domain walls, *Phys. Chem. Chem. Phys.* 22 (26) (2020) 14415–14432.
- [2] S. Picozzi, K. Yamauchi, I.A. Sergienko, C. Sen, B. Sanyal, E. Dagotto, Microscopic mechanisms for improper ferroelectricity in multiferroic perovskites: a theoretical review, *J. Phys. Condens. Matter* 20 (2008) 1–10.
- [3] S. Tomic, M. Dressel, Ferroelectricity in molecular solids: a review of electrodynamic properties, *Rep. Prog. Phys.* 78 (9) (2015) 1–26.
- [4] H.C. Wu, Chuang Zhou, Remarkable enhancement in hybrid improper ferroelectricity of $\text{Ca}_3\text{Ti}_2\text{O}_7$ ceramics by a simple sol-gel process, *Mater. Lett.* 278 (2020) 1–4.

- [5] O.S. Es-Said, D.O. Urroz-Montoya, J.R. Alverto-Suazo, J.R. Garcia-Cabrera, C.H. Ortega-Jimenez, P. Jisheng, Piezoelectricity: a literature review for power generation support, *Mateconf* 293 (2019) 1–6.
- [6] M. Mohammadkhah, D. Marinkovic, M. Zehn, S. Checa, A review on computer modeling of bone piezoelectricity and its application to bone adaptation and regeneration, *Bone* 127 (2019) 544–555.
- [7] S. Education, Symmetry-based electricity in minerals and rocks: a review with examples of centrosymmetric minerals that exhibit pyroand piezoelectricity, *Period. Mineral.* 85 (2016) 201–248.
- [8] M. Marvan, J. Fousek, Pyroelectricity and compositionally graded ferroelectrics: a brief review of our theoretical approach, *Phase Transitions* 79 (6–7) (2006) 485–492.
- [9] T. Ali, A study on the temperature-dependent operation of fluorite-structure-based ferroelectric HfO₂ memory FeFET: pyroelectricity and reliability, *Nanomater. Energy* 67 (7) (2020) 2981–2987.
- [10] J.L. Liu, S. L.H. Liu, Origin of pyroelectricity in ferroelectric HfO₂, *Phys. Rev. Applied.* 12 (3) (2019) 1–10.
- [11] V.S. Bystrov, Piezoelectricity and pyroelectricity in hydroxyapatite, *Ferroelectrics* 541 (1) (2019) 25–29.
- [12] D.O. Carvalho, L.R.P. Kassab, V.D. Del Cacho, D.M. da Silva, M.I. Alayo, A review on pedestal waveguides for low loss optical guiding, optical amplifiers and nonlinear optics applications, *J. Lumin.* 203 (2018) 135–144.
- [13] P. Gong, X. Liu, L. Kang, Z. Lin, Inorganic planar π -conjugated groups in nonlinear optical crystals: review and outlook, *Inorg. Chem. Front.* 7 (4) (2020) 839–852.
- [14] S.K. Yesodha, C.K. Sadashiva Pillai, N. Tsutsumi, Stable polymeric materials for nonlinear optics: a review based on azobenzene systems, *Prog. Polym. Sci.* 29 (1) (2004) 45–74.
- [15] L.H. Gao, Junben, Siru Guo, Structure-property survey and computer-assisted screening of mid-infrared nonlinear optical chalcogenides, *Coord. Chem. Rev.* 421 (2020) 1–28.
- [16] W. Wang, D. Mei, F. Liang, J. Zhao, Y. Wu, Z. Lin, Inherent laws between tetrahedral arrangement pattern and optical performance in tetrahedron-based mid-infrared nonlinear optical materials, *Coord. Chem. Rev.* 421 (2020) 1–13.
- [17] K. Wu, Y. Yang, L. Gao, A review on phase transition and structure-performance relationship of second-order nonlinear optical polymorphs, *Coord. Chem. Rev.* 418 (2020) 1–25.
- [18] Y. Liu, Y. Shen, S. Zhao, J. Luo, Structure-property relationship in nonlinear optical materials with π -conjugated CO₃ triangles, *Coord. Chem. Rev.* 407 (2020) 1–20.
- [20] A. Iyo, H. Fujihisa, Y. Gotoh, S. Ishida, H. Ninomiya, Y. Yoshida, H. Eisaki, H.T. Hirose, T. Terashima, K. Kawashima, Structural phase transitions and superconductivity induced in antiperovskite phosphide CaPd₃P, *Inorg. Chem.* 59 (17) (2020) 12397–12403.
- [21] P. Szperlich, M. Nowak, L. Bober, J. Szala, D. Stroz, Ferroelectric properties of ultrasonochemically prepared SbSI ethanogel, *Ultrason. Sonochem.* 16 (3) (2009) 398–401.
- [22] Atsushi Kikuchi¹, Oka¹. Yoshio, Sawaguchi¹. Etsuro, Crystal structure determination of SbSI, *J. Phys. Soc. Jpn.* 23 (1967) 2.
- [23] K. Hamano, Piezoelectric property of SbSI single crystal, *J. Phys. Soc. Jpn.* 20 (1965) 10.
- [24] D.S. Grekov Aa, P.L. Zaks, V.V. Kuliava, L.A. Rubanov, S. Ln, Piezoelectric elements made from antimony sulphoiodide crystals, *Akust. Zhurnal* 19 (1973) 622–623.
- [25] J.R. Xiao, S.H. Yang, F. Feng, H.G. Xue, S.P. Guo, A review of the structural chemistry and physical properties of metal chalcogenide halides, *Coord. Chem. Rev.* 347 (2017) 23–47.
- [26] G.M. Sheldrick, Crystal structure refinement with SHELXL, *Acta Crystallogr. Sect. C-Struct. Chem.* 71 (2015) 3–8.
- [27] S.K. Perry, A powder technique for the evaluation of nonlinear optical materials, *J. Appl. Phys.* 39 (1968) 3798–3813.
- [28] G. Kresse, From ultrasoft pseudopotentials to the projector augmented-wave method, *Phys. Rev. B* 77 (1996) 1758–1775.
- [29] G. Kresse, From ultrasoft pseudopotentials to the projector augmented-wave method, *Phys. Rev. B* 59 (1999) 1758–1775.
- [30] J. Perdew, Kieron, Matthias Ernzerhof, Generalized gradient approximation made simple, *Phys. Rev. Lett.* 77 (1996) 1396, 1396.
- [31] M.N. Sotome, M. J. Fujioka, M. Ogino, Y. Kaneko, T. Morimoto, Y. Zhang, M. Kawasaki, N. Nagaosa, Y. Tokura, N. Ogawa, Spectral dynamics of shift current in ferroelectric semiconductor SbSI, *Proc. Natl. Acad. Sci. U.S.A.* 116 (6) (2019) 1929–1933.